ACS APPLIED MATERIALS & INTERFACES

Research Article

Cite This: ACS Appl. Mater. Interfaces 2018, 10, 11715−11721

www.acsami.org

Systematic Study of Oxygen Evolution Activity and Stability on $La_{1-x}Sr_xFeO_{3-\delta}$ Perovskite Electrocatalysts in Alkaline Media

Sixuan She,[†] Jie Yu,[†] Wanqi Tang,[†] Yinlong Zhu,[†] Yubo Chen,[‡] Jaka Sunarso,[§] Wei Zhou,*[,†] and Zongping Shao*[,†,∥]

[†]Jiangsu National Synergetic Innovation Center for Advanced Materials (SICAM), State Key Laboratory of Materials-Oriented Chemical Engineering, College of Chemical Engineering, Nanjing Tech University, No. 5 Xin Mofan Road, Nanjing 210009, P. R. China

[‡]School of Material Science and Engineering, Nanyang Technological University, 50 Nanyang Avenue, 639798 Singapore, Singapore

[§]Faculty of Engineering, Computing and Science, Swinburne University of Technology, Jalan Simpang Tiga, 93350 Kuching, Sarawak, Malaysia

[∥]Department of Chemical Engineering, Curtin University, Perth, Western Australia 6845, Australia

Supporting Information

ABSTRACT: Perovskite oxide is an attractive low-cost alternative catalyst for oxygen evolution reaction (OER) relative to the precious metal oxide-based electrocatalysts (IrO_2 and RuO_2). In this work, a series of Sr-doped La-based perovskite oxide catalysts with compositions of $La_{1-x}Sr_xFeO_{3-\delta}$ (x = 0, 0.2, 0.5, 0.8, and 1) are synthesized and characterized. The OER-specific activities in alkaline solution increase in the order of $LaFeO_{3-\delta}$ (LF), $La_{0.8}Sr_{0.2}FeO_{3-\delta}$ (LSF-0.2), $La_{0.5}Sr_{0.5}FeO_{3-\delta}$ (LSF-0.5), $SrFeO_{3-\delta}$ (SF), and $La_{0.2}Sr_{0.8}FeO_{3-\delta}$ (LSF-0.8). We establish a direct correlation between the enhancement in the specific activity and the amount of surface oxygen vacancies as well as the surface Fe oxidation states. The improved specific activity for LSF-0.8 is clearly linked to the optimum amount of surface oxygen vacancies and surface Fe oxidation states. We also find that the OER performance stability is a function of the crystal structure and the deviation in the surface La and/or Sr composition(s) from their bulk stoichiometric compositions. The cubic structure and lower deviation, as is the case for LSF-0.8, led to a higher OER performance stability. These surface performance relations provide a promising guideline for constructing efficient water oxidation.

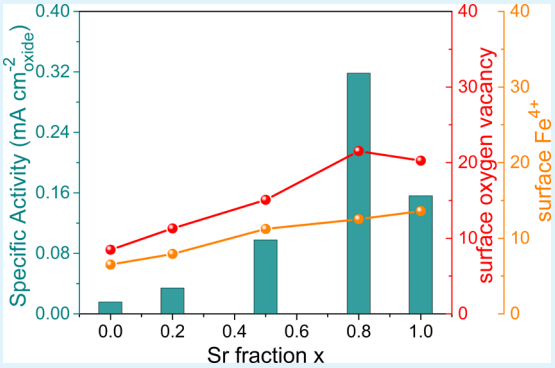

KEYWORDS: *$La_{1-x}Sr_xFeO_{3-\delta}$, oxygen evolution reaction, surface oxygen vacancies, surface Fe oxidation states, structure*

INTRODUCTION

Oxygen evolution reaction (OER) is an essential process for diverse energy conversion and storage devices including water splitting, regenerative fuel cells, and rechargeable metal−air batteries.[1−3] The sluggish kinetics of the reaction in the absence of electrocatalyst generally manifests in large overpotential, leading to significant energy consumption.[4−6] The presence of effective electrocatalysts such as IrO_2 and RuO_2 can minimize such overpotentials; however, these precious metal oxides are not applicable for large-scale applications given their high costs and inferior stability.[7−9] The development of more abundant low-cost electrocatalysts as an alternative to these metal oxides has thus become a central goal of most research and development studies on this topic.[10−14]

Perovskite oxide, that is, a compound with a compositional formula of ABO_3, where A is an alkaline earth or rare-earth metal cation and B is a transition-metal cation, has become one of the most promising candidates because of its structural and compositional flexibility.[1,15−17] The enhancement in electrocatalytic activities in the past has focused on the incorporation of different metal components of different amounts into the A-site and B-site lattice positions of the perovskite oxide.[18−21] More recently, it has been discovered that key descriptors such as the M−OH bond strengths, e_g electron configuration, surface affinity to the oxygen species, and O p-band energy levels can predict trends in electrocatalytic activities.[22−25] The application of an accurate electronic property descriptor that relies upon density functional theory and molecular orbital theory, in particular, may assist the design and development of the high-performance OER catalysts in the near future.

$LaFeO_3$ is one of the most widely used parent compositions in the perovskite family for applications such as sensors, visible-light photocatalysis, and catalysts in solid oxide fuel cells.[26−28] $LaFeO_3$ displays low electrochemical activity in an alkaline

Received: January 13, 2018
Accepted: March 16, 2018
Published: March 16, 2018

DOI: 10.1021/acsami.8b00682
ACS Appl. Mater. Interfaces 2018, 10, 11715−11721

solution.[23−25] To improve the electrochemical activity, La^{3+} cations can be partially substituted by metal cations with a lower oxidation state, such as Sr^{2+}.[32,33] Zhu et al. recently reported that A-site cation-deficient $La_{0.95}FeO_{3-\delta}$ showed simultaneously high OER and oxygen reduction reaction activities in an alkaline solution.[34] Furthermore, Schuhmann and co-workers reported that $La_{0.6}Sr_{0.4}FeO_{3-\delta}$ exhibited high OER activity in an alkaline solution, whereas $La_{0.58}Sr_{0.4}FeO_{3-\delta}$ featured negligible OER activity.[35] These results suggest the significant effect of the stoichiometry variation on the OER activity, which requires further systematic study.[29−31]

In the following study, a series of $La_{1-x}Sr_xFeO_{3-\delta}$ (LSF-x, where x = 0, 0.2, 0.5, 0.8, and 1) catalysts were synthesized for investigating the OER, of which $La_{1-x}Sr_xFeO_{3-\delta}$ with x = 0.8 exhibited the best performance. The surface property change in Sr-doped $LaFeO_3$ was investigated, and the enhanced specific activity was linked directly to the amount of surface oxygen vacancies and surface Fe oxidation states. The crystal structure additionally appears to affect the OER stability, with the cubic structure providing the best stability over the orthorhombic and tetragonal structures. X-ray photoelectron spectroscopy (XPS) also indicated that the stable compositions have close to a stoichiometric amount of La and Sr on their surfaces. As a result, the optimized Sr doping in $LaFeO_3$ promoted the OER performance.

EXPERIMENTAL SECTION

Material Synthesis. $La_{1-x}Sr_xFeO_{3-\delta}$ (LSF-x, where x = 0, 0.2, 0.5, 0.8, and 1) powders were prepared by following a synthetic procedure reported before.[10] In brief, 80 mL of ammonia solution dissolved with 0.1 mol of ethylenediaminetetraacetic acid was well-mixed under vigorous stirring into a solution containing a mixture of $La(NO_3)_3\cdot 6H_2O$ (0.05−0.05 × x mol), $Sr(NO_3)_2$ (0.05 × x mol), and $Fe(NO_3)_3\cdot 9H_2O$ (0.05 mol). Subsequently, citric acid (0.2 mol) was added into the above mixture. The resulting homogeneous mixture was heated at 90 °C with continuous stirring until a transparent gel was obtained, which was prefired at 250 °C to form a foamlike solid precursor. Finally, the solid precursors of LSF-x were further heated to 800 °C at a rate of 5 °C min^{-1} and maintained at 800 °C for 5 h.

Characterization. The crystallographic information on the LSF-x samples was recorded by a powder X-ray diffractometer equipped with a Cu Kα source (Bruker D8 ADVANCE) at a step rate of 20° min^{-1} from 10° to 90°. The Rietveld refinements (GSAS software and the EXPGUI interface) were adopted to further determine the space groups as well as the lattice parameters of these samples. The microstructure images were observed via a field emission scanning electron microscope (Hitachi S-4800). The specific surface areas were calculated using the Brunauer−Emmett−Teller (BET) method, and pore-size distributions were analyzed on a N_2 adsorption−desorption instrument (BELSORP-mini, Japan) at a liquid nitrogen temperature (77 K). The iodometric titration described in a previous report was performed to obtain the oxygen nonstoichiometry and Fe average oxidation state of the product.[34] The chemical compositions were identified through XPS using a PHI5000 system, and surface elemental states were quantified by the area of fitted spectra using XPSPEAK41 software.

Electrode Preparation. Twenty milligrams of the measured material [containing 10 mg of the as-prepared LSF-x powder and 10 mg of conductive carbon (Super P Li)] and 100 μL of 5 wt % Nafion solution were ultrasonically dispersed in 1 mL of absolute ethanol. Five microliters of the catalyst ink (0.232 mg_{cat} cm^{-2}) was then transferred onto the surface of the glassy carbon (0.196 cm^2) substrate and dried at room temperature for 1 h.

Electrochemical Measurements. The electrocatalytic properties were investigated in a three-electrode electrochemical cell connected with a rotating disk electrode (RDE) configuration (Pine Research Instrumentation). The data were collected using a CHI 760E bipotentiostat. The reference electrode was saturated Ag/AgCl (3.5 M KCl) (0.95 V vs the reversible hydrogen electrode (RHE) in 0.1 M KOH), and a platinum wire served as the counter electrode. During the electrochemical measurements, the electrolyte was purged with a flow of O_2 to ensure its continued O_2 saturation. Prior to each test, cyclic voltammograms (CVs) obtained at a sweep rate of 100 mV s^{-1} were carried out in the potential region from 0.2 to −1.2 V (vs Ag/AgCl) at 1600 rpm until the curves completely overlapped. Linear sweep voltammetry (LSV), namely, polarization curve, was recorded through sweeping the potential from 0.2 to 1.0 V (vs Ag/AgCl) at a scan rate of 5 mV s^{-1} at 1600 rpm. The Tafel was taken as the value of the slope obtained from plotting the potential near the onset potential as a function of the logarithm of current density. The scan rate dependence of CVs (20, 40, 60, 80, 100, and 120 mV s^{-1}) measured in a potential region of 0.2−0.3 V (vs Ag/AgCl) was collected to estimate the double-layer capacitance (C_{dl}). The electrochemical impedance spectroscopy (EIS) measurements were performed at 0.7 V (vs Ag/AgCl) under the influence of an alternating current (ac) voltage of 5 mV from 100 kHz to 0.1 Hz. The stability of the samples was studied by comparing the LSV profiles before and after a given number of cycles of continuous CV scans at a 10 mV s^{-1} scan rate. All potential values shown were calibrated to RHE after being iR-corrected using the following equation: E(RHE) = E(Ag/AgCl) − 0.95 V.

RESULTS AND DISCUSSION

Figure 1a shows the powder X-ray diffraction (XRD) patterns of the $La_{1-x}Sr_xFeO_{3-\delta}$ (LSF-x, where x = 0, 0.2, 0.5, 0.8, and 1) powders synthesized using a sol−gel route. These powders are denoted as LF, LSF-0.2, LSF-0.5, LSF-0.8, and SF. The positions of the characteristic peaks are shifted to higher angles with an increase in the strontium content (x), which indicates a lattice size reduction at higher strontium contents. Because the ionic radius of Sr^{2+} (1.44 Å) is larger than that of La^{3+} (1.36 Å), such a lattice reduction likely comes from the oxidation of Fe^{3+} (0.645 Å) to Fe^{4+} (0.585 Å) due to charge compensation when Sr^{2+} substitutes for La^{3+}.[36] Table 1 lists the lattice parameters and the reliability factors obtained from Rietveld refinements of

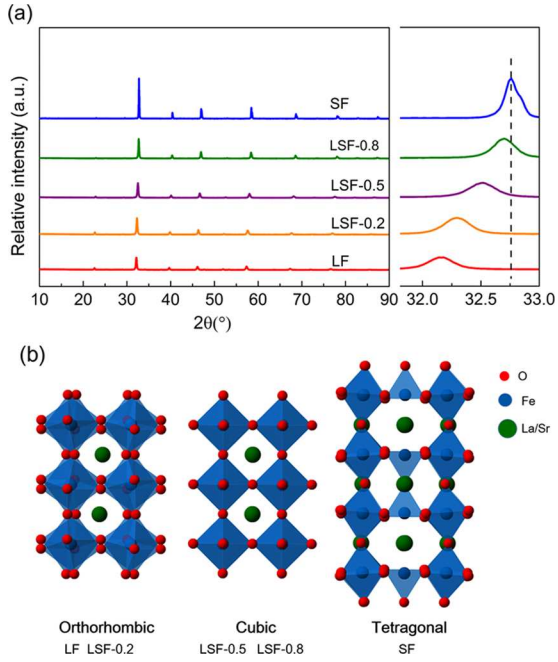

Figure 1. (a) Powder XRD patterns, with an expanded region of 2θ = 32°−33° shown on the right, and (b) schematic structures of the LSF-x (x = 0, 0.2, 0.5, 0.8, and 1) powders.

DOI: 10.1021/acsami.8b00682
ACS Appl. Mater. Interfaces 2018, 10, 11715−11721

Table 1. Lattice Parameters of LF, LSF-0.2, LSF-0.5, LSF-0.8, and SF from Rietveld Refinements of Their Powder XRD Patterns

		LF	LSF-0.2	LSF-0.5	LSF-0.8	SF
space group (no.)		*Pnma* (#62)	*Pnma* (#62)	$Pm\bar{3}m$(#221)	$Pm\bar{3}m$(#221)	$I4/mmm$(#139)
lattice parameters (Å)	*a*	5.5606(5)	5.5297(8)	3.8910(6)	3.8684(3)	10.9331(1)
	b	7.8539(5)	7.826(1)	3.8910(6)	3.8684(3)	10.9331(1)
	c	5.5689(5)	5.5538(9)	3.8910(6)	3.8684(3)	7.7154(1)
bond length (Å)	$Fe-O_1$	1.9822	1.9994	1.9455	1.9342	1.9211
	$Fe-O_2$	1.8234/2.1684	1.8103/2.1311			
R_p		5.43%	3.66%	3.88%	3.76%	4.75%
R_{wp}		6.12%	4.17%	4.22%	4.18%	6.18%
χ^2		1.537	1.292	1.234	1.306	2.091

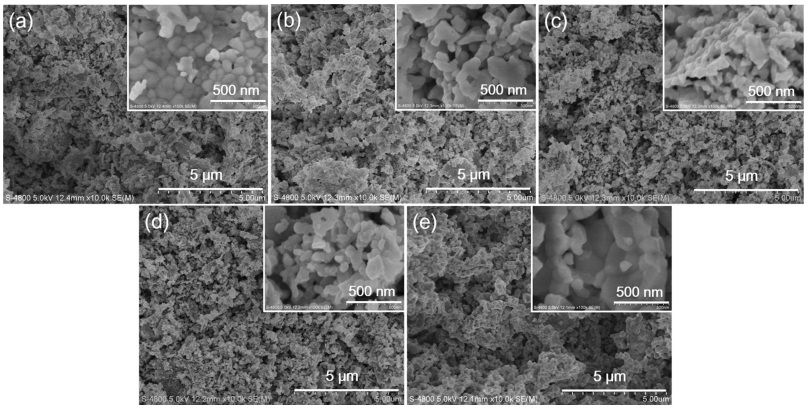

Figure 2. FE-SEM images of the LSF-*x* (x = 0, 0.2, 0.5, 0.8, and 1) powders, that is, (a) LF; (b) LSF-0.2; (c) LSF-0.5; (d) LSF-0.8; and (e) SF. Scale bar—5 mm. The inset figures show the magnified images. Scale bar—500 nm.

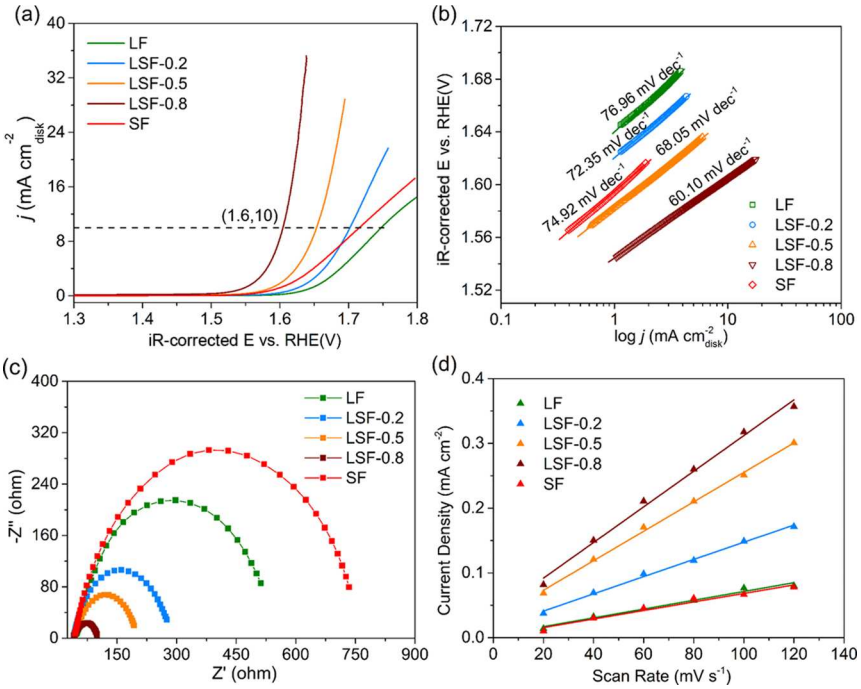

Figure 3. (a) OER polarization profiles for the LSF-*x* (x = 0, 0.2, 0.5, 0.8, and 1) samples obtained using a 5 mV s^{-1} scan rate in an O_2-saturated 0.1 M KOH solution; (b) respective Tafel plots; (c) electrochemical impedance spectra for the LSF-*x* (x = 0, 0.2, 0.5, 0.8, and 1) samples obtained at 0.7 V vs Ag/AgCl; and (d) current densities at 0.25 V vs Ag/AgCl as a functions of scan rate for the LSF-*x* (x = 0, 0.2, 0.5, 0.8, and 1) samples.

the powder XRD patterns. LF and LSF-0.2 exhibited an orthorhombic lattice with a *Pnma* space group (#62), whereas LSF-0.5 and LSF-0.8 featured a primitive cubic lattice with a $Pm\bar{3}m$ space group (#221). SF, on the other hand, adopted a tetragonal lattice with an $I4/mmm$ space group (#139) (Figure 1b). Partial substitution of La^{3+} by Sr^{2+} thus facilitates the progressive structure change from orthorhombic to cubic structure, the increase in the oxygen nonstoichiometry (δ), and the change in the oxidation state of iron (Fe) (Table S1—obtained from the iodometric titrations). In the SF case, the

DOI: 10.1021/acsami.8b00682
ACS Appl. Mater. Interfaces 2018, 10, 11715−11721

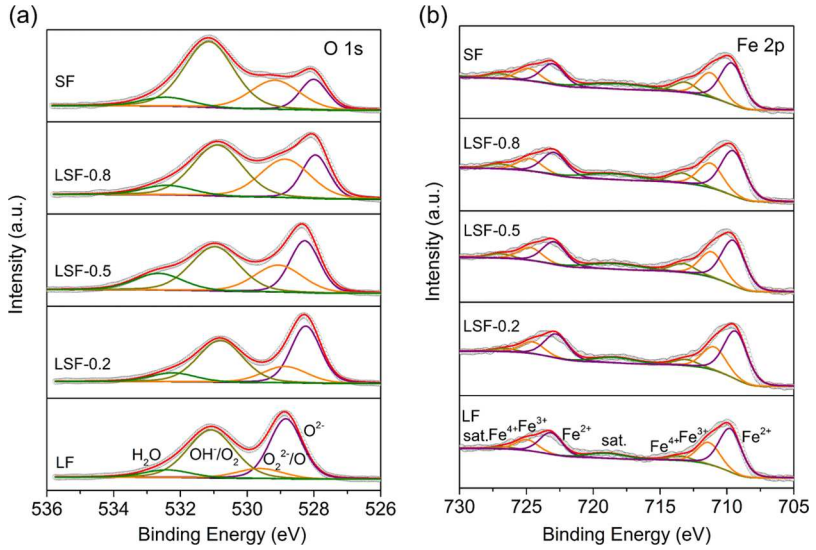

Figure 4. (a) O 1s and (b) Fe 2p X-ray photoelectron spectra of the LSF-x (x = 0, 0.2, 0.5, 0.8, and 1) powders.

presence of a large amount of oxygen vacancies, as reflected by its highest oxygen nonstoichiometry among the five compositions, leads to the adoption of a tetragonal lattice instead of a cubic lattice, which is consistent with the previous report.[37]

The surface morphologies of the LSF-x (x = 0, 0.2, 0.5, 0.8, and 1) powders were probed using field emission scanning electron microscopy (FE-SEM), and the results are displayed in Figure 2. Submicron particles are observed together forming several agglomerates. Except for SF, which shows the largest particle size, for other compositions, the particle size appears to decrease with an increase in Sr content, in agreement with the previous report.[38] This trend is additionally supported by the enlargement of the BET specific surface area with an increase in the Sr content from LF to LSF-0.8 (Table S2). SF showed the lowest surface area of 2.0 $m^2\ g^{-1}$ among the five compositions because of its highest sinterability. In general, a higher surface area provides more active sites for the reactions, which should promote OER electrochemical performance.

The OER activities of the LSF-x (x = 0, 0.2, 0.5, 0.8, and 1) samples were evaluated using a RDE at 1600 rpm in 0.1 M KOH electrolyte (reference electrode Ag/AgCl). All potentials shown were referenced to the RHE (see Figure S2 for RHE calibration). Figure 3a shows the typical LSV profiles taken at a 5 mV s^{-1} scan rate and 1600 rpm rotation rate. LSF-0.8 displayed the lowest onset potential of ∼1.54 V among the five compositions, followed by LSF-0.5 of ∼1.58 V, SF of ∼1.59 V, LSF-0.2 of ∼1.62 V, and LF of ∼1.64 V. The overpotential (η) to achieve a current density of 10 mA cm^{-2} represents a performance metric relevant to 10% efficient solar-to-fuel conversion, which is necessary to evaluate the performance of OER electrocatalysts. LSF-0.8 showed an overpotential value of 0.37 V, which is 50, 100, 110, and 140 mV lower than those values for LSF-0.5, LSF-0.2, SF, and LF, respectively. The superior OER performance of LSF-0.8 among the five compositions is also evident from its largest OER current density at any particular potential. For example, at 1.63 V versus RHE, LSF-0.8 delivered an OER current density of 26 mA cm^{-2}, which is ∼43-, ∼19-, ∼10-, and ∼5-fold greater than those for LF, LSF-0.2, SF, and LSF-0.5, respectively. To gain further insights into the catalysts, Tafel plots and EIS spectra recorded at 0.7 V (vs Ag/AgCl) are displayed in Figure 3b,c, respectively. LSF-0.8 displayed a much smaller Tafel slope and a semicircular diameter in the EIS spectra, suggesting a rapid reaction rate and highly efficient electron transport during the OER reaction.

The electrochemically active surface areas (ECSAs) of LF, LSF-0.2, LSF-0.5, LSF-0.8, and SF were estimated using the electrochemical double-layer capacitance (C_{dl}) measurements, the results of which are shown in Figure 3d. The obtained C_{dl} of LSF-0.8 was 2.75 mF cm^{-2}, which is larger than those of LSF-0.5 (2.27 mF cm^{-2}), LSF-0.2 (1.33 mF cm^{-2}), LF (0.68 mF cm^{-2}), and SF (0.66 mF cm^{-2}). This ECSA trend is identical to that of the BET surface area trend (Table S2). To remove the surface area effect from the OER activity, the OER current densities were normalized against the BET surface area of the respective samples. At 1.6 V, LSF-0.8 displayed a specific current density of 0.32 mA cm_{oxide}^{-2}, which is 20.4-, 9.3-, 3.2-, and 2-fold greater than those for LF (0.016 mA cm_{oxide}^{-2}), LSF-0.2 (0.034 mA cm_{oxide}^{-2}), LSF-0.5 (0.098 mA cm_{oxide}^{-2}), and SF (0.16 mA cm_{oxide}^{-2}). The mismatch between this trend and the ECSA trend rules out the notion that the ECSA is the key factor behind the superior OER performance of LSF-0.8.

Such a superior performance is likely attributed to two other factors. The first factor is the surface oxygen vacancies. As noted above, the presence of oxygen vacancies in Sr-doped LSF-x perovskites as measured by a bulk iodometric titration method affords more opportunities for oxygen ion diffusion, which can be demonstrated by the diffusion rate of oxygen ions (Figure S3). However, there is no direct correlation between the oxygen ion diffusion rate and the specific activity. Therefore, we have investigated the surface oxygen vacancies because the catalytic reaction occurs at the surface of the heterogeneous systems. Previous studies have shown that the formation of highly oxidative oxygen species (O_2^{2-}/O^-) on the catalyst surface was closely related to the surface oxygen vacancies,[39,40] which were also active for OER.[10,41] On the basis of these findings, the surface oxygen species of the LSF-x (x = 0, 0.2, 0.5, 0.8, and 1) powders were characterized using XPS. The O 1s spectra for LF, LSF-0.2, LSF-0.5, LSF-0.8, and SF consist of two major components: the low-energy components correspond to the lattice oxygen (O^{2-}) and the high-energy components are attributed to the surface phases (Figure 4a).[42] Generally, the latter ranked dependent on energy from low to high are highly oxidative oxygen (O_2^{2-}/O^-), adsorbed oxygen

DOI: 10.1021/acsami.8b00682
ACS Appl. Mater. Interfaces 2018, 10, 11715−11721

(OH^-/O_2), adsorbed H_2O, or carbonates on the surface (Figure 4a). Table S4 lists the relative amount of these four species in the five compositions calculated from the relative areas of their deconvoluted peaks. As seen, the O_2^{2-}/O^- species content increases in the order of LF < LSF-0.2 < LSF-0.5 < SF < LSF-0.8. The similarity between the trends shown by the specific activities and the surface oxygen vacancies suggests that surface oxygen vacancies are an important factor for determining the OER performance (Figure 5). The second

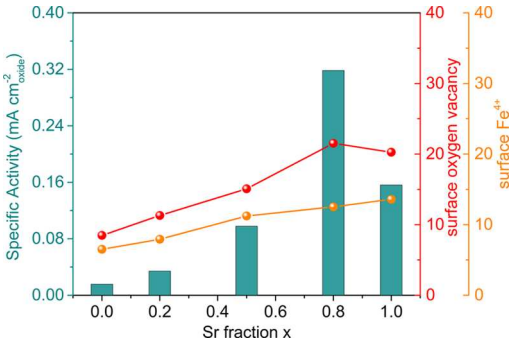

Figure 5. Relationship between specific activities and surface oxygen vacancies and surface Fe oxidation states for the LSF-x (x = 0, 0.2, 0.5, 0.8, and 1) samples.

factor is the presence of Fe^{4+} species on the surface. We determined the oxidation state of Fe using Fe 2p XPS spectra of the five samples (LF, LSF-0.2, LSF-0.5, LSF-0.8, and SF), which are displayed in Figure 4b.[34] Table S3 details the relative amounts of different Fe species as estimated from the relative area of their subpeaks. The relative amount of Fe^{4+} seems to increase with increasing Sr content, following the order LF < LSF-0.2 < LSF-0.5 < LSF-0.8 < SF. Because of the strong binding energy of Fe^{4+} to the reaction intermediate species (*OH) in the OER, excessive Fe^{4+} can hinder the detachment of OH^- and subsequent oxygen gas release.[13] It can be anticipated that the favorable Fe oxidation state exists and provides an appropriate binding strength for reaction intermediates to the LSF-x surface, thus resulting in an optimized OER performance. Figure 5 plots the specific activity, which exhibited a "volcano" trend with increasing Sr concentration, confirming the presence of optimized Fe oxidation states. Overall, it appears that the OER performance of LSF-x correlates with the surface oxygen vacancies and the surface Fe oxidation states.

The stability of OER performance is also important for practical application. We determined the operational durability of the LSF-x samples by comparing the LSV profiles before and after 20 cycles of continuous CV scans at a 10 mV s^{-1} scan rate. The potential difference at a current density of 3 mA cm^{-2} (ΔV) was measured and is displayed in Figure 6. The ΔV values for LF, LSF-0.2, LSF-0.5, LSF-0.8, and SF are 20.63, 11.02, 4.41, 3.41, and 21.20 mV, respectively. LSF-0.5 and LSF-0.8, which exhibit a cubic structure, showed the lowest degradation in OER performance among the five samples. The retainment of OER performance over the long OER cycles may be closely related to the surface segregation of the A-site cations, that is, La and/or Sr. XPS data show that LF and LSF-0.2, which have an orthorhombic structure, had significantly higher La molar content than their bulk stoichiometric composition in their surfaces (Table 2). LSF-0.2 also had substantially lower Sr content than its bulk stoichiometric composition in its surface (Table 2). Much less discrepancy relative to their bulk stoichiometric compositions nonetheless was observed for LSF-0.5 and LSF-0.8, which exhibit a cubic structure. We attribute the surface segregation of La and Sr in LF and LSF-0.2 as the main factor that limits their long-term

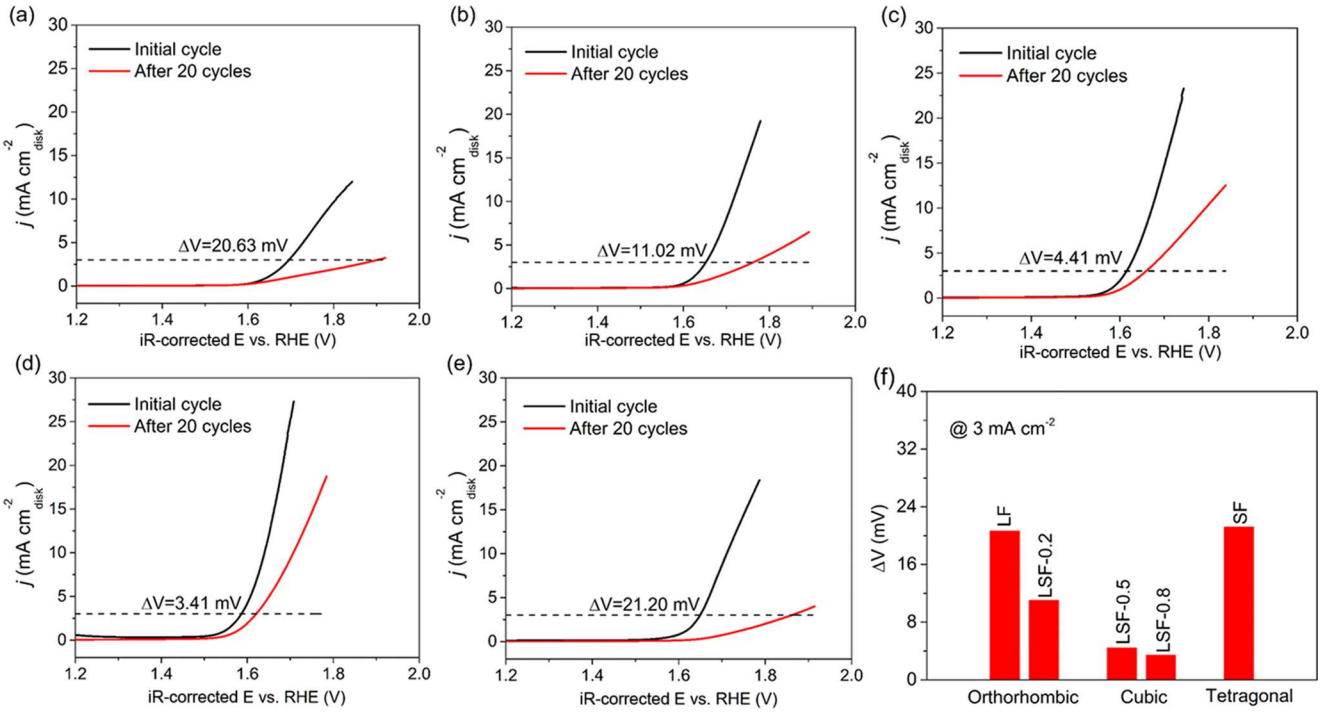

Figure 6. OER polarization profiles before and after 20 continuous OER cycles for (a) LF; (b) LSF-0.2; (c) LSF-0.5; (d) LSF-0.8; and (e) SF and (f) potential difference at a current density of 3 mA cm^{-2} (ΔV) for the LSF-x (x = 0, 0.2, 0.5, 0.8, and 1) samples.

DOI: 10.1021/acsami.8b00682
ACS Appl. Mater. Interfaces 2018, 10, 11715−11721

Table 2. XPS-Derived Atomic Compositional Data for the LSF-x (x = 0, 0.2, 0.5, 0.8, and 1) Samples[a]

samples	La 3d	Sr 3d	Fe 2p
LF	74.16% (50%)		25.84% (50%)
LSF-0.2	54.82% (30%)	11.20% (20%)	33.98% (50%)
LSF-0.5	34.24% (25%)	24.25% (25%)	41.51% (50%)
LSF-0.8	19.08% (20%)	32.97% (30%)	47.94% (50%)
SF		53.59% (50%)	46.41% (50%)

[a]La 3d % + Sr 3d % + Fe 2p % = 100% (the values in brackets represent the bulk stoichiometric compositions).

OER stability, the details of which require further specific study. In the SF case, OER performance degradation is likely caused by the phase transition during the repeated OERs.[43] Our observation here suggests the beneficial effect of having a cubic structure to obtain stable OER performance.

CONCLUSIONS

The surface properties of $La_{1-x}Sr_xFeO_{3-\delta}$ (x = 0, 0.2, 0.5, 0.8, and 1) perovskites were explored for water oxidation. Gradual substitution of La^{3+} by Sr^{2+} leads to the change of surface oxygen vacancies and surface Fe oxidation states, which go hand in hand with the significant enhancement of water oxidation activity. Among these five samples, LSF-0.8 displayed the lowest OER overpotential, the most negative OER onset potential, and the lowest Tafel slope. The overpotential of LSF-0.8 at a 10 mA cm^{-2} current density can reach a level of 0.37 V. Moreover, the crystal structure and the deviation of surface La and Sr composition from the bulk stoichiometric composition appear to affect the OER performance stability over 20 continuous OER cycles. Cubic LSF-0.5 and LSF-0.8 lower deviation displayed the lowest degradation in OER performance during such cycles. These new perspectives make strongly correlated surface properties promising for the systematic exploration of surface−performance relation in heterogeneous catalysis.

ASSOCIATED CONTENT

Supporting Information

The Supporting Information is available free of charge on the ACS Publications website at DOI: 10.1021/acsami.8b00682.

$La_{1-x}Sr_xFeO_{3-\delta}$ perovskite structural characterizations, for example, Rietveld refinements of XRD patterns, iodometric titrations, BET, and XPS; potential calibration of the reference electrode (Ag/AgCl); and diffusion rate of oxygen ion analyses during electrocatalytic tests (PDF)

AUTHOR INFORMATION

Corresponding Authors

*E-mail: zhouwei1982@njtech.edu.cn. Phone: +86 25 83172256. Fax: +86 25 83172242 (W.Z.).

*E-mail: shaozp@njtech.edu.cn. Phone: +86 25 83172256. Fax: +86 25 83172242 (Z.S.).

ORCID

Jaka Sunarso: 0000-0002-5234-7431

Wei Zhou: 0000-0003-0322-095X

Zongping Shao: 0000-0002-4538-4218

Notes

The authors declare no competing financial interest.

ACKNOWLEDGMENTS

This work was financially supported by the National Natural Science Foundation of China under no. 21576135, Jiangsu Natural Science Foundation for Distinguished Young Scholars (no. BK20170043), the Priority Academic Program Development of Jiangsu Higher Education Institutions, the Program for Changjiang Scholars, the Program for Jiangsu Specially-Appointed Professors, and the Youth Fund in Jiangsu Province (no. BK20150945).

REFERENCES

(1) Chen, D.; Chen, C.; Baiyee, Z. M.; Shao, Z.; Ciucci, F. Nonstoichiometric Oxides as Low-Cost and Highly-Efficient Oxygen Reduction/Evolution Catalysts for Low-Temperature Electrochemical Devices. *Chem. Rev.* **2015**, *115*, 9869−9921.

(2) Xiao, Z.; Wang, Y.; Huang, Y.-C.; Wei, Z.; Dong, C.-L.; Ma, J.; Shen, S.; Li, Y.; Wang, S. Filling the Oxygen Vacancies in Co_3O_4 with Phosphorus: an Ultra-Efficient Electrocatalyst for Overall Water Splitting. *Energy Environ. Sci.* **2017**, *10*, 2563−2569.

(3) Wang, Y.; Zhang, Y.; Liu, Z.; Xie, C.; Feng, S.; Liu, D.; Shao, M.; Wang, S. Layered Double Hydroxide Nanosheets with Multiple Vacancies Obtained by Dry Exfoliation as Highly Efficient Oxygen Evolution Electrocatalysts. *Angew. Chem.* **2017**, *129*, 5961−5965.

(4) Gorlin, Y.; Jaramillo, T. F. A Bifunctional Nonprecious Metal Catalyst for Oxygen Reduction and Water Oxidation. *J. Am. Chem. Soc.* **2010**, *132*, 13612−13614.

(5) Zhang, J.; Zhao, Z.; Xia, Z.; Dai, L. A Metal-Free Bifunctional Electrocatalyst for Oxygen Reduction and Oxygen Evolution Reactions. *Nat. Nanotechnol.* **2015**, *10*, 444−452.

(6) Sun, H.; Chen, G.; Zhu, Y.; Liu, B.; Zhou, W.; Shao, Z. B-Site Cation Ordered Double Perovskites as Efficient and Stable Electrocatalysts for Oxygen Evolution Reaction. *Chem.—Eur. J.* **2017**, *23*, 5722−5728.

(7) Petrykin, V.; Macounova, K.; Shlyakhtin, O. A.; Krtil, P. Tailoring the Selectivity for Electrocatalytic Oxygen Evolution on Ruthenium Oxides by Zinc Substitution. *Angew. Chem., Int. Ed.* **2010**, *49*, 4813−4815.

(8) Jiao, Y.; Zheng, Y.; Jaroniec, M.; Qiao, S. Z. Design of Electrocatalysts for Oxygen- and Hydrogen-Involving Energy Conversion Reactions. *Chem. Soc. Rev.* **2015**, *44*, 2060−2086.

(9) Liu, R.; Wang, Y.; Liu, D.; Zou, Y.; Wang, S. Water-Plasma-Enabled Exfoliation of Ultrathin Layered Double Hydroxide Nanosheets with Multivacancies for Water Oxidation. *Adv. Mater.* **2017**, *29*, 1701546.

(10) Zhu, Y.; Zhou, W.; Chen, Y.; Yu, J.; Liu, M.; Shao, Z. A High-Performance Electrocatalyst for Oxygen Evolution Reaction: $LiCo_{0.8}Fe_{0.2}O_2$. *Adv. Mater.* **2015**, *27*, 7150−7155.

(11) Anantharaj, S.; Ede, S. R.; Sakthikumar, K.; Karthick, K.; Mishra, S.; Kundu, S. Recent Trends and Perspectives in Electrochemical Water Splitting with an Emphasis on Sulfide, Selenide, and Phosphide Catalysts of Fe, Co, and Ni: A Review. *ACS Catal.* **2016**, *6*, 8069−8097.

(12) Wang, J.; Cui, W.; Liu, Q.; Xing, Z.; Asiri, A. M.; Sun, X. Recent Progress in Cobalt-Based Heterogeneous Catalysts for Electrochemical Water Splitting. *Adv. Mater.* **2016**, *28*, 215−230.

(13) Chen, G.; Zhou, W.; Guan, D.; Sunarso, J.; Zhu, Y.; Hu, X.; Zhang, W.; Shao, Z. Two Orders of Magnitude Enhancement in Oxygen Evolution Reactivity on Amorphous $Ba_{0.5}Sr_{0.5}Co_{0.8}Fe_{0.2}O_{3-\delta}$ Nanofilms with Tunable Oxidation State. *Sci. Adv.* **2017**, *3*, No. e1603206.

(14) Dou, S.; Dong, C.-L.; Hu, Z.; Huang, Y.-C.; Chen, J.-l.; Tao, L.; Yan, D.; Chen, D.; Shen, S.; Chou, S.; Wang, S. Atomic-Scale CoO_x Species in Metal−Organic Frameworks for Oxygen Evolution Reaction. *Adv. Funct. Mater.* **2017**, *27*, 1702546.

(15) Tiwari, S. K.; Singh, S. P.; Singh, R. N. Effects of Ni, Fe, Cu, and Cr Substitutions for Co in $La_{0.8}Sr_{0.2}CoO_3$ on Electrocatalytic

Properties for Oxygen Evolution. *J. Electrochem. Soc.* **1996**, *143*, 1505−1510.
(16) Hwang, J.; Rao, R. R.; Giordano, L.; Katayama, Y.; Yu, Y.; Shao-Horn, Y. Perovskites in Catalysis and Electrocatalysis. *Science* **2017**, *358*, 751−756.
(17) Xu, X.; Su, C.; Zhou, W.; Zhu, Y.; Chen, Y.; Shao, Z. Co-doping Strategy for Developing Perovskite Oxides as Highly Efficient Electrocatalysts for Oxygen Evolution Reaction. *Adv. Sci.* **2016**, *3*, 1500187.
(18) Jörissen, L. Bifunctional Oxygen/Air Electrodes. *J. Power Sources* **2006**, *155*, 23−32.
(19) Du, Z.; Yang, P.; Wang, L.; Lu, Y.; Goodenough, J. B.; Zhang, J.; Zhang, D. Electrocatalytic Performances of $LaNi_{1-x}Mg_xO_3$ Perovskite Oxides as Bi-Functional Catalysts for Lithium Air Batteries. *J. Power Sources* **2014**, *265*, 91−96.
(20) Shimizu, Y.; Matsuda, H.; Miura, N.; Yamazoe, N. Bi-functional Oxygen Electrode Using Large Surface Area Perovskite-Type Oxide Catalyst for Rechargeable Metal-Air Batteries. *Chem. Lett.* **1992**, *21*, 1033−1036.
(21) Duan, Y.; Sun, S.; Xi, S.; Ren, X.; Zhou, Y.; Zhang, G.; Yang, H.; Du, Y.; Xu, Z. J. Tailoring the Co 3d-O 2p Covalency in $LaCoO_3$ by Fe Substitution to Promote Oxygen Evolution Reaction. *Chem. Mater.* **2017**, *29*, 10534−10541.
(22) Subbaraman, R.; Tripkovic, D.; Chang, K.-C.; Strmcnik, D.; Paulikas, A. P.; Hirunsit, P.; Chan, M.; Greeley, J.; Stamenkovic, V.; Markovic, N. M. Trends in Activity for the Water Electrolyser Reactions on 3D M(Ni,Co,Fe,Mn) Hydr(oxy)oxide Catalysts. *Nat. Mater.* **2012**, *11*, 550−557.
(23) Suntivich, J.; May, K. J.; Gasteiger, H. A.; Goodenough, J. B.; Shao-Horn, Y. A Perovskite Oxide Optimized for Oxygen Evolution Catalysis from Molecular Orbital Principles. *Science* **2011**, *334*, 1383−1385.
(24) Rossmeisl, J.; Qu, Z.-W.; Zhu, H.; Kroes, G.-J.; Nørskov, J. K. Electrolysis of Water on Oxide Surfaces. *J. Electroanal. Chem.* **2007**, *607*, 83−89.
(25) Grimaud, A.; May, K. J.; Carlton, C. E.; Lee, Y.-L.; Risch, M.; Hong, W. T.; Zhou, J.; Shao-Horn, Y. Double Perovskites as a Family of Highly Active Catalysts for Oxygen Evolution in Alkaline Solution. *Nat. Commun.* **2013**, *4*, 2439.
(26) Natile, M. M.; Ponzoni, A.; Concina, I.; Glisenti, A. Chemical Tuning versus Microstructure Features in Solid-State Gas Sensors: LaFe1-xGaxO3, a Case Study. *Chem. Mater.* **2014**, *26*, 1505−1513.
(27) Thirumalairajan, S.; Girija, K.; Hebalkar, N. Y.; Mangalaraj, D.; Viswanathan, C.; Ponpandian, N. Shape Evolution of Perovskite $LaFeO_3$ Nanostructures: A Systematic Investigation of Growth Mechanism, Properties and Morphology Dependent Photocatalytic Activities. *RSC Adv.* **2013**, *3*, 7549−7561.
(28) Maguire, E.; Gharbage, B.; Marques, F. M. B.; Labrincha, J. A. Cathode Materials for Intermediate Temperature SOFCs. *Solid State Ionics* **2000**, *127*, 329−335.
(29) Sunarso, J.; Torriero, A. A. J.; Zhou, W.; Howlett, P. C.; Forsyth, M. Oxygen Reduction Reaction Activity of La-Based Perovskite Oxides in Alkaline Medium: A Thin-Film Rotating Ring-Disk Electrode Study. *J. Phys. Chem. C* **2012**, *116*, 5827−5834.
(30) Wang, Y.; Cheng, H.-P. Oxygen Reduction Activity on Perovskite Oxide Surfaces: A Comparative First-Principles Study of $LaMnO_3$, $LaFeO_3$, and $LaCrO_3$. *J. Phys. Chem. C* **2013**, *117*, 2106−2112.
(31) Lee, Y.-L.; Gadre, M. J.; Shao-Horn, Y.; Morgan, D. Ab Initio GGA+U Study of Oxygen Evolution and Oxygen Reduction Electrocatalysis on the (001) Surfaces of Lanthanum Transition Metal Perovskites $LaBO_3$ (B = Cr, Mn, Fe, Co and Ni). *Phys. Chem. Chem. Phys.* **2015**, *17*, 21643−21663.
(32) Duprat, A. M.; Alphonse, P.; Sarda, C.; Rousset, A.; Gillot, B. Nonstoichiometry-Activity Relationship in Perovskite-like Manganites. *Mater. Chem. Phys.* **1994**, *37*, 76−81.
(33) Read, M. S. D.; Islam, M. S.; Watson, G. W.; King, F.; Hancock, F. E. Defect Chemistry and Surface Properties of LaCoO3. *J. Mater. Chem.* **2000**, *10*, 2298−2305.
(34) Zhu, Y.; Zhou, W.; Yu, J.; Chen, Y.; Liu, M.; Shao, Z. Enhancing Electrocatalytic Activity of Perovskite Oxides by Tuning Cation Deficiency for Oxygen Reduction and Evolution Reactions. *Chem. Mater.* **2016**, *28*, 1691−1697.
(35) Rincón, R. A.; Ventosa, E.; Tietz, F.; Masa, J.; Seisel, S.; Kuznetsov, V.; Schuhmann, W. Evaluation of Perovskites as Electrocatalysts for the Oxygen Evolution Reaction. *ChemPhysChem* **2014**, *15*, 2810−2816.
(36) Shannon, R. D. Revised Effective Ionic Radii and Systematic Studies of Interatomic Distances in Halides and Chalcogenides. *Acta Crystallogr., Sect. A: Cryst. Phys., Diffr., Theor. Gen. Crystallogr.* **1976**, *32*, 751−767.
(37) Dann, S. E.; Currie, D. B.; Weller, M. T.; Thomas, M. F.; Al-Rawwas, A. D. The Effect of Oxygen Stoichiometry on Phase Relations and Structure in the System $La_{1-x}Sr_xFeO_{3-\delta}$ ($0 \le x \le 1$, $0 \le \delta \le 0.5$). *J. Solid State Chem.* **1994**, *109*, 134−144.
(38) Kafa, C. A.; Triyono, D.; Laysandra, H. Effect of Sr Substitution on the Room Temperature Electrical Properties of $La_{1-x}Sr_xFeO_3$ Nano-Crystalline Materials. *AIP Conf. Proc.* **2017**, *1862*, 030042.
(39) Zhu, J.; Li, H.; Zhong, L.; Xiao, P.; Xu, X.; Yang, X.; Zhao, Z.; Li, J. Perovskite Oxides: Preparation, Characterizations, and Applications in Heterogeneous Catalysis. *ACS Catal.* **2014**, *4*, 2917−2940.
(40) Merino, N. A.; Barbero, B. P.; Eloy, P.; Cadús, L. E. $La_{1-x}Ca_xCoO_3$ Perovskite-Type Oxides: Identification of the Surface Oxygen Species by XPS. *Appl. Surf. Sci.* **2006**, *253*, 1489−1493.
(41) Liu, R.; Liang, F.; Zhou, W.; Yang, Y.; Zhu, Z. Calcium-Doped Lanthanum Nickelate Layered Perovskite and Nickel Oxide Nano-Hybrid for Highly Efficient Water Oxidation. *Nano Energy* **2015**, *12*, 115−122.
(42) Yu, J.; Sunarso, J.; Zhu, Y.; Xu, X.; Ran, R.; Zhou, W.; Shao, Z. Activity and Stability of Ruddlesden−Popper-Type $La_{n+1}Ni_nO_{3n+1}$ (n=1, 2, 3, and ∞) Electrocatalysts for Oxygen Reduction and Evolution Reactions in Alkaline Media. *Chem.—Eur. J.* **2016**, *22*, 2719−2727.
(43) Nemudry, A.; Weiss, M.; Gainutdinov, I.; Boldyrev, V.; Schöllhorn, R. Room Temperature Electrochemical Redox Reactions of the Defect Perovskite $SrFeO_{2.5+x}$. *Chem. Mater.* **1998**, *10*, 2403−2411.

DOI: 10.1021/acsami.8b00682
ACS Appl. Mater. Interfaces 2018, 10, 11715−11721